Atmospheric
Chemistry
and Physics
Discussions

Open Access

Forecasting Carbon Monoxide on a Global Scale for the ATom-1 Aircraft Mission: Insights from Airborne and Satellite Observations and Modeling

Sarah A. Strode[1,2], Junhua Liu[1,2], Leslie Lait[2,3], Róisín Commane[4], Bruce Daube[4], Steven Wofsy[4], Austin Conaty[2,5], Paul Newman[2], Michael Prather[6]

[1]Universities Space Research Association, Columbia, MD, USA

[2]NASA GSFC, Greenbelt, MD, USA

[3]Morgan State University, Baltimore, MD, USA

[4]Harvard University, Cambridge, MA, USA

[5]SSAI, Greenbelt, MD, USA

[6]University of California, Irvine, CA, USA

Correspondence to: Sarah A. Strode (sarah.a.strode@nasa.gov)

Abstract GEOS-5 forecasts and analyses show considerable skill in predicting and simulating the CO distribution and the timing of CO enhancements observed during the ATom-1 aircraft mission. Using tagged tracers for CO, we find a dominant contribution from non-biomass burning sources along the ATom transects except over the tropical Atlantic, where African biomass burning makes a large contribution to the CO concentration. One of the goals of ATom is to provide a chemical climatology over the oceans, so it is important to consider whether August 2016 was representative of typical summer conditions. Using satellite observations of 700 hPa and column CO from the Measurement of Pollution in the Troposphere (MOPITT) instrument, 215 hPa CO from the Microwave Limb Sounder (MLS), and aerosol optical thickness from the Moderate Resolution Imaging Spectroradiometer (MODIS), we find that CO concentrations and aerosol optical thickness in Aug. 2016 were within the observed range of the satellite observations, but below the decadal median for many of the regions sampled. This suggests that the ATom-1 measurements may represent relatively clean but not exceptional conditions for lower tropospheric CO.

Atmospheric
Chemistry
and Physics
Discussions

1 Introduction

The first phase of the NASA Atmospheric Tomography Mission (ATom-1) took place in July-August 2016. The aircraft completed a circuit beginning in Palmdale, California and traversing the remote Pacific and Atlantic oceans, providing an unprecedented picture of the chemical environment at a wide range of latitudes over the remote oceans. Chemical forecasts from the GEOS-5 model provided insight into the chemical environments and sources of pollution for the diverse regions sampled during the ATom-1 campaign.

ATom provides an observation-based climatology of important atmospheric constituents and their reactivity in the remote atmosphere. *Prather et al.* (2017) examined the ability of observations from a single path to represent the variability of a broader geographic region, but noted that year-to-year and El Nino/Southern Oscillation (ENSO) variability could also be important. Here we show how the time and place of ATom-1 measurements fit into a global, multi-year climatology of CO.

Year to year variability in meteorology and emissions both contribute to interannual variability in trace gases and aerosols. For example, ENSO is a major driver of variability in ozone distributions (*Ziemke and Chandra*, 2003), and large biomass burning events during El Nino years increase concentrations of trace gases including CO and CO_2 (*Langenfelds et al.*, 2002). Biomass burning plays a particularly strong role in driving the interannual variability of CO (e.g. *Novelli et al.*, 2003; *Kasischke et al.*, 2005; *Duncan and Logan*, 2008; *Strode and Pawson*, 2013; *Voulgarakis et al.*, 2015;). The impacts of large biomass burning events during El Nino events are visible in satellite observations of CO (e.g. *Edwards et al.*, 2004; *Edwards et al.*, 2006; *Logan et al.*, 2008, *Liu et al.*, 2013).

Pfister et al. (2010) used a chemistry transport model (CTM) as well as satellite data to examine the CO sources and transport over the Pacific during the INTEX-B mission compared to previous years. They found biomass burning to be the largest contributor to interannual variability, despite its lower emissions compared to fossil fuel sources.

In this study, we place the August 2016 ATom observations in the context of interannual variability and assess the contributions of different emission sources to the various regions sampled during the campaign. We focus on CO, a tracer of incomplete combustion whose lifetime of 1-2 months allows long-range transport to the remote oceans. Section 2 describes the model and observations used in this analysis. Section 3 compares the GEOS-5 CO to observations. Section 4 discusses the global distribution of CO, and presents the relative CO source contributions to the regions sampled by ATom. Section 5 presents an analysis of the interannual variability in CO and aerosol optical thickness seen in satellite observations to assess how well August 2016 observations represent climatological August conditions. Section 6 summarizes our conclusions.

Atmospheric
Chemistry
and Physics
Discussions

2   Observations and Model

2.1   ATom Observations

ATom-1 flew transects through the Pacific, Southern, Atlantic and Arctic oceans with the NASA
DC8 aircraft in August 2016. Each of the 11 flights included sampling from the boundary layer to the top
of the aircraft range (39 kft). We use the ATom-1 data (July-August 2016) [*Atom Science Team,* 2017] for
comparison with the model forecasts and analyses.

We take ATom-1 CO observations from the Harvard QCLS instrument (*Santoni et al*., 2014), which
has a history of successful measurements during the HIAPER Pole-to-Pole Observations (HIPPO)
campaign. Briefly, the instrument uses a pulsed quantum cascade laser at 2160 cm^{-1} to measure absorption
of CO through a astigmatic multi-pass sample cell (with 76 m path length), with detection using liquid
nitrogen cooled HgCdTe detector. A separate laser and detector are used to measure methane and nitrous
oxide in the same cell. Inflight calibrations were conducted with gases traceable to the NOAA WMO
(X2014) scale, with calibration of tanks before ATom1 and after ATom2 (February 2017) showing no
significant change in the CO concentration in the gas standards. The inlet for the instrument was specially
designed   for   the   DC-8   aircraft.

2.2   Satellite Observations

We use satellite observations that cover more than a decade to examine the interannual variability
of CO and aerosols. The Measurement of Pollution in the Troposphere (MOPITT) instrument, which flies
on the Terra satellite, provides CO observations beginning in 2000 (*Edwards et al*., 2004). We use the
version 6 thermal infrared (TIR) level 3 product (*Deeter et al.,* 2014). The MOPITT TIR averaging kernels
show high sensitivity to CO between 700 and 500 hPa (*Emmons et al.*, 2007).

The Microwave Limb Sounder (MLS) (*Waters et al*., 2006), which flies on the Aura satellite,
provides useful observations of CO down to 215 hPa (*Livesey et al.,* 2008) beginning in 2004. We use the
Version 4.2 level 2 data with the recommended quality, status, precision, and convergence criteria.
Although MLS data overlap with ATom only at the highest flight levels, both it and MOPITT provide
complementary views of CO in the lower troposphere and upper troposphere/lower stratosphere (UTLS),
respectively.

The Moderate Resolution Imaging Spectroradiometer (MODIS) instrument on the Aqua satellite
provides column aerosol optical thickness (AOT) data beginning in 2002. We use the Collection-6 level 2
(MYD04_L2) [*Levy et al.*, 2015] 550 nm AOT data over oceans aggregated into 0.5 degree grid boxes, and
then take monthly means with the daily data weighted according to the QA.

2.3   Model Description

We use chemical forecasts and analyses from the GEOS-5 Forward Processing (FP) system. The FP
stream from the Global Modeling and Assimilation Office (GMAO) generates GEOS-5 forecast products as

98   well as assimilation products using the most current system approved for near-real-time production. The

99   GEOS-5 model (*Molod et al.*, 2015) is a global general circulation model (GCM) with 72 vertical levels

100   reaching from the surface to 1 Pa. The assimilation system is described in (*Rienecker et al.*, 2008;

101   *Rienecker et al.,* 2011), and includes assimilation of ozone measurements from the Ozone Monitoring

102   Instrument (OMI) and MLS, and aerosol optical depth as well as meteorological variables. The forward

103   processing system produces output on 72 model levels or 42 pressure levels with 5/16 by 1/4 degree

104   horizontal resolution. Our study uses the pressure level output.

105   The GEOS-5 FP system (*Lucchesi*, 2017) simulates the transport of CO as well as tagged CO tracers

106   from specific regions and sources, which helps track the transport of pollution outflow. Tagged tracers are

107   available for biomass burning (BB) globally as well as biomass burning from Eurasia, North America,

108   Africa, and Central and South America; and for non-BB sources globally and from Europe, Asia, and North

109   America. Non-BB sources include fossil fuels, biofuels, CO from oxidation of biogenic VOCs, and CO

110   from methane oxidation, as described in *Ott et al.* (2010). *Bian et al.* (2013) used observations of

111   dichloromethane and acetonitrile from the ARCTAS mission to validate the anthropogenic and biomass

112   burning CO tracers, respectively.

113   Daily-varying biomass burning emissions come from the Quick Fire Emission Dataset (QFED)

114   version 2 [*Darmenov and da Silva*, 2015], which is based on fire radiative power from the MODIS

115   instrument. Thus the BB emissions include day-to-day and interannual variability, but the non-BB sources

116   and the OH fields use monthly means and lack daily-scale variability and interannual variability. Table 1

117   presents the August emission inputs for the major regions considered. CO emissions are then scaled up by

118   20% for fossil fuels and 11% for biomass burning to account for CO production from co-emitted VOCs.

119   CO from methane oxidation is included in the non-BB tagged tracers for the regions in which oxidation

120   occurred. The monthly mean methane fields come from a GMI Chemistry and Transport Model (CTM)

121   simulation, which uses prescribed zonal mean surface concentrations. CO is lost by reaction with OH

122   using fixed monthly OH fields archived from the GMI CTM. Supplemental Figure S1 shows the methane

123   and OH fields included in the FP system.

124   **3   GEOS-5 Chemical Forecasting for ATom**

125   During the ATom mission, the GEOS-5 model is engaged to provide chemical forecasts for each

126   flight that include the major chemical species and, for CO, tagged tracers for different sources. The

127   chemical forecasts are used together with meteorological forecasts for day-to-day flight planning, although

128   flight tracks were intentionally not altered to chase specific chemical features to avoid a highly biased

129   sampling of pollution.

130   We examine the performance of the GEOS-5 forecasts by comparing the simulated CO to the QCLS

131   observations. The forecasts provided during the mission used forecast wind fields, with the forecast lead

132   time varying depending on the timing of the flight. For consistency, the results shown here use the CO

133   simulated with the assimilated wind fields, but we note that similar features were seen for the CO simulated

Atmospheric
Chemistry
and Physics
Discussions

134   with the forecast winds, as further discussed in section 3.1.2. For the model results, we do not apply

135   temporal interpolation between the model output frequency (6 hours). Instead, we sample the model

136   forecasts at the time closest to the mid-point of each flight segment. To compare with observations, the 3D

137   model forecast was interpolated to the longitude, latitude and pressure given in the 10-second merges of the

138   ATom measurements.

139   **3.1   Analysis of CO along the Meridional Flight Tracks**

140   We compare CO from GEOS-5 to the QCLS CO observations for specific flights, using the 10-

141   second merge files. The GEOS-5 CO is taken from the 3D field at the time closest to the mid-point of the

142   flight and interpolated in space to the flight track. We focus on two sections of the ATom-1 circuit: the

143   North to South flights through the Pacific, and the South to North flights through the Atlantic, although we

144   briefly discuss the other flights as well. These two transects allow us to examine the transition from

145   northern hemispheric to tropical to southern hemispheric influence.

146   **3.1.1   Pacific legs**

147   Figure 1 shows CO from the three Pacific flights spanning Anchorage, Alaska to Christchurch,

148   New Zealand. The top panels show the GEOS-5 curtain of CO along the flight track, with the QCLS

149   observations overplotted in circles. The observations show higher values of CO in the first half of the

150   Anchorage-Kona flight compared to the other portions of the Pacific, and this feature is reproduced in

151   GEOS-5 as well. GEOS-5 agrees well with the observed mean value for CO on this flight (Table 2).

152   Tagged tracers (Fig. 1 bottom panels) show that non-BB sources, especially from Asia, are the dominant

153   contributor to CO levels throughout the Pacific, and the decrease in Asian non-BB CO explains the

154   observed decrease in CO as the flights move south.

155   The observations show plumes of enhanced CO scattered throughout all three Pacific flights,

156   although they are most intense in the north Pacific, as seen in the Anchorage-Kona flight. GEOS-5

157   typically reproduces the timing of these plumes, but the magnitude is usually underestimated, particularly

158   for the strongest plumes. This leads to an underestimate of the observed standard deviation of the CO on

159   the Palmdale-Anchorage (Fig. S2) and Anchorage-Kona flights (Table 2). In addition to biases in

160   emissions, observations often show fine-scale structures too small for the model to resolve (Hsu et al.,

161   2004), and underestimating the concentrations in strong plumes is a common problem for global models

162   (e.g. *Heald et al.*, 2003). An exception is in the tropical Pacific (Kona-Pago Pago flight), in which GEOS-5

163   predicted some enhancements, driven by fossil fuels, not seen in the observations. Tagged tracers indicate

164   that Asian non-BB CO drove many of the observed enhancements, while others were due to biomass

165   burning.

166   In the south Pacific (Pago Pago to Christchurch segment), the flight sampled the stratosphere three

167   times, with CO levels decreasing to approximately 30 ppb, as shown in Fig. 1c. As expected from the basic

168   chemistry and seen in previous observations, both ATom-1 and GEOS-5 show a strong decrease in CO as

169   the flight rises above the tropopause, with GEOS-5 underestimating the observed decrease. Both the model

170 and measurements show tropospheric CO less than 90 ppbv along the flight route with slightly elevated CO

171 above 600 hPa around T22:00 and T24:00. For this flight and the subsequent flight to Punta Arenas, all

172 observations are in the Southern Hemisphere and the mean values for both ATom-1 and GEOS-5 agree

173 within the range 54-57 ppb (Table 2, Fig S3).

3.1.2 Atlantic Legs

175 The ATom flights traversed the Atlantic from South to North, beginning in Punta Arenas, Chile

176 and ending in Kangerlussuaq, Greenland. Figure 2 shows the Atlantic flights from Punta Arenas to

177 Ascension Island to the Azores to Kangerlussuaq. GEOS-5 has an excellent simulation of background CO

178 values seen on these flights, with the mean values falling within 2 ppb of the observations (Table 2) while

179 the mean observed values for each flight shift from 69 to 101 to 88 ppb. The observations show plumes of

180 high CO intersecting the flight track on all three flights. GEOS-5 also shows plumes of enhanced CO at

181 these locations, but the magnitude is often underestimated (Fig. 2d-f), especially for the Azores-

182 Kangerlussuaq flight. Supplemental Figure S4 shows the CO results for the Azores-Kangerlussuaq flight

183 using forecast wind fields, and illustrates the temporal evolution of CO plumes along the flight track.

184 Comparison of Fig. S4 with Fig. 2f shows the small impact of using analysis versus forecast wind fields.

185 Non-BB sources dominate the background CO levels on all three flights. However, biomass

186 burning plays a dominant role in the plumes of high CO (Fig. 2g-i). South American biomass burning

187 leads to CO enhancements between T14 and T16 of the Punta Arenas to Ascension flight. In the later

188 portion of that flight, biomass burning from Africa leads to strong CO plumes. Strong plumes of African

189 biomass burning are also seen at the beginning of the Ascension to Azores flight. GEOS-5 shows a strong

190 plume around 800 hPa for the first hour of the flight, which agrees well with observations (Fig. 2b,d). The

191 observations show additional strong plumes in the next hour between 600 and 700 hPa. These plumes are

192 present but underestimated in GEOS-5, possibly due to errors in the magnitude of the emissions or the

193 placement of the plumes.

194 The non-BB contribution to CO in the Atlantic reflects a mixture of global sources. Asian sources

195 make a notable contribution to the non-BB CO variability in the tropics (first half of the Ascension to

196 Azores flight), but as expected N. American sources become more dominant in the second half. In the

197 northern (later) portion of the Azores to Kangerlussuaq flight (Fig. 2), GEOS-5 attributes the observed

198 plumes to Eurasian biomass burning, but underestimates their magnitude. This flight also crosses the

199 tropopause, and both ATom-1 and GEOS-5 show a corresponding dip in CO concentrations. GEOS-5

200 predicts a plume of enhanced CO due to N. American emissions around 11Z of the Azores to

201 Kangerlussuaq flight that is not seen in the observations (Fig. 2f,i). A similar error is made in the

202 Kangerlussuaq to Minneapolis flight (Fig. S3). This could be due to either an error in the assumed N.

203 American sources, or to misplacement of the plume by the model. A large overestimate of CO at the end of

204 the Minneapolis to Palmdale flight also points to a potential error in North American emissions from either

205 fossil fuels or biomass burning.

Atmospheric
Chemistry
and Physics
Discussions

3.2   Model Evaluation Summary

206
207   We summarize the comparison between the CO simulated by the GEOS-5 analyses and the QCLS
208   observations in Figure 3. The majority of points lie near the one-to-one line, indicating good overall
209   agreement between the GEOS-5 and observed CO distributions. The higher concentrations in the tropical
210   Atlantic compared to the tropical Pacific are evident in both the observations and model. Fig. 3 also
211   reveals occasional model overestimates of CO on flights over North America (green triangles), as well as
212   underestimates of high CO plumes over the North Pacific and Tropical Atlantic. An underestimate of
213   Eurasian biomass burning contributes to the model underestimates in the North Pacific and North Atlantic,
214   and has implications for ozone production in aged BB plumes [*Liu et al*., in prep]. Globally, the correlation
215   of simulated and observed CO with 5-minute binning is r=0.69. Correlations for the Pacific, Atlantic, and
216   North America are 0.72, 0.80, and 0.80, respectively, while the correlation for the southern ocean is 0.053.
217   The poor correlation for the southern ocean reflects the very low variability of CO in this region. The
218   model performs far better at capturing the larger gradients present in the other regions. In general, the good
219   agreement between model outputs and observations testify the model forecasting skill and suggest the
220   suitability of using GEOS-5 forecast products to guide the design and execution of aircraft campaigns.

4   Source Contributions to the Global CO Distribution

4.1   Global CO Distribution

223   Figure 4 compares CO from GEOS-5 to the QCLS CO observations for the ATom-1 circuit including
224   the 11 total flight segments. The GEOS-5 CO is taken from the analysis closest to the mid-point of the
225   flight time and interpolated to the flight track following the longitude, latitude and pressure given in the
226   observations. We average both model CO and ATom measurements into one point per 360-seconds for
227   easier visualization.
228   Both model simulations and measurements show polluted air with higher CO mixing ratios in the
229   northern hemisphere than that in the southern hemisphere in August 2016. Over the northern hemispheric
230   polar region, the observations indicate highly polluted air with CO maxima occurring over Alaska and
231   northwest Canada, features also seen in the GEOS-5 simulation. Over the Atlantic section, CO maxima
232   with slightly lower values occur around the same latitude over west Greenland as shown both in
233   observations and model simulation. CO over the northern most locations along the ATom-1 circuit see
234   some low values both in model and observations, particularly north of 30°N and south of 40°S, due to the
235   measurements occuring in the stratosphere or occurring in the upper troposphere with stratospheric
236   influence. Both model and observations indicate that the air is relatively clean over the Pacific south of 30N
237   with CO less than 70 ppb and the CO minimum around 60S over the southeast Pacific. Over the Atlantic
238   section, both model and observations show low CO concentration south of 30S, but show a strong CO
239   maximum over the tropical Atlantic (5S-5N) with CO greater than 120 ppb. This high CO is mainly driven
240   by southern hemisphere BB. CO is slightly lower between 30N and 60N compared to that over tropical

Atmospheric
Chemistry
and Physics
Discussions

241   Atlantic and the Greenland. The similarity between GEOS-5 and ATom-1 variability in neighboring points

242   is due in part to the vertical profiling which places horizontally extensive biomass burning layers in both

243   model and presumably the atmosphere at the same point along the track.

244   **4.2   CO Source Contributions**

245   We calculate the contribution of different CO sources to the total simulated CO using the GEOS-5

246   tagged CO tracers sampled along the ATom flight tracks. This analysis provides a picture of the dominant

247   sources affecting the constituent concentrations observed during ATom-1 for different regions of the

248   atmosphere. The tagging of CO sources includes both biomass burning (BB) and non-biomass burning

249   (non-BB) from four continental areas, with all other sources put into the "other" bin. Other BB sources are

250   small, but other non-BB sources are quite large as they include all natural sources as well as atmospheric

251   photochemical sources such as methane oxidation.

252   Figure 5 shows the contribution of each tagged tracer over the Pacific Ocean from 120°E to 110°W,

253   averaged over 5 degree latitude bins. Non-biomass burning sources dominate at all latitudes, due in part to

254   the inclusion of CO from methane oxidation in addition to fossil fuel sources in these tracers. The

255   oxidation of methane over the remote oceans contributes to the large magnitude of "other non-BB" sources

256   over the southern latitudes of the Pacific. Asian non-BB sources make the largest contribution to middle

257   and upper tropospheric CO (Fig. 5a) at the mid-latitudes of the North Pacific, with smaller contributions

258   from N. American and European non-BB sources. The largest biomass burning contribution comes from

259   Africa in the Southern Hemisphere and Tropics, switching to Eurasia in the northern latitudes.

260   Figure 5b shows the relative contributions in the lower troposphere, including the marine boundary

261   layer and defined here as pressures greater than 850 hPa. Missing bars indicate latitudes where no ATom-1

262   measurements were made in the lower troposphere. Asian non-BB CO makes a smaller contribution in the

263   lower troposphere than in the middle and upper troposphere. A strong CO maximum around 30°N is more

264   pronounced in the lower troposphere than above. This bin is not representative of the remote Pacific as it

265   includes Palmdale, California, with large contributions from local North American BB and non-BB

266   sources.

267   The Atlantic flights (0°-60°W) show a large contribution from other non-BB sources in the

268   Southern Hemisphere with increasing contributions from Asian, N. American, and European non-BB CO

269   as the flight moves northward (Fig. 6), similar to the picture over the Pacific. However, the Atlantic

270   receives a larger contribution from biomass burning, particularly from Africa, over the Tropics. The

271   contribution from African BB is strong throughout the troposphere, but is particularly pronounced in the

272   lower troposphere, where it exceeds 100 ppb in the bins centered at 10°S and 5°N.

273   We also examine the tagged tracer contributions for each flight, including all altitudes sampled by

274   the flight (Fig. 7, Supp. Table S1). Flights occurring in the tropics and southern hemisphere (Flt. 1, 4-8)

275   receive 44-75% of the total CO from other non-BB sources. Other non-biomass burning sources include all

276   non-biomass burning sources located outside North America, Europe, and Asia. The contribution from

277   methane oxidation in addition to southern hemisphere emissions explains this large contribution. Flight 8

278   has a somewhat lower percent contribution from other non-BB sources than the other southern hemisphere

279   and tropical flights due to the higher percent contribution from African biomass burning. In contrast, the

280   Northern Hemisphere flights have a larger contribution from northern hemisphere source regions. Asian

281   non-BB explains over a third of the total CO for the northern Pacific flights (Flt. 2-3), while Asian and N.

282   American non-BB sources make comparable contributions to the North Atlantic and N. American flights

283   (Flt. 9-11).

284   Since Figs. 5 and 6 reveal differences in source contributions between the lower troposphere and the

285   middle and upper troposphere, we also examine the source contributions to each flight for the lower

286   troposphere (Pressure > 850 hPa) only (Supp. Fig. S5). Asian sources make a larger percent contribution to

287   the Pacific flights (Flt. 0-4) when all flight altitudes are considered rather than the lower troposphere alone.

288   Regional sources such as African biomass burning for flights 6 and 7 and N. American sources for Flights 9

289   and 10 make a larger percent contribution in the lower troposphere.

290   **5   August 2016 in the Context of Interannual Variability (IAV)**

291   One of the major goals for the ATom campaign is to produce a climatology based on un-biased,

292   representative samples (*Prather et al.*, 2017). It is therefore important to consider whether August 2016 is

293   a "typical" summer month.   We focus here on the temporal representativeness of the ATom-1 campaign.

294   Spatial representativeness is investigated in *Liu et al.* [in prep]. August of 2016 was ENSO neutral, with a

295   multivariate ENSO index (MEI) (*Wolter and Timlin*, 1993); (https://www.esrl.noaa.gov/psd/enso/mei) of

296   0.175 for July/August.   However, it was preceded by strong El Nino conditions in 2015 and early 2016

297   (*Blunden and Arndt*, 2016).   We therefore consider whether the CO concentrations in August 2016 are

298   typical or anomalous.

299   Multi-year satellite records provide a valuable tool for determining how CO concentrations in the

300   regions of the ATom-1 flights compare to previous years.   We focus our analysis of CO interannual

301   variability on several regions traversed by the ATom flights. Figure 8 shows these regions in black squares

302   overplotted on the MOPITT CO column for August 2016. We also examine the IAV in BB sources from

303   nearby regions, outlined in red on Fig. 8. Figure 9 shows box-and-whisker plots of the mean, minimum,

304   25th, 50th, and 75th percentiles, and maximum in monthly mean August CO for each region over the 2000-

305   2016 period for MOPITT (CO column and CO at 700 hPa) and 2004-2016 for MLS (CO at 215 hPa). The

306   corresponding time series are shown in Fig. 10. The variability in CO BB emissions from GFEDv4 for

307   2000-2016 is also shown for BB regions that may affect the ATom flights. The BB emissions are averaged

308   over June through August to account for the persistence of CO in the atmosphere.

309   Among the regions mapped here, the tropical Atlantic shows the highest average CO values, as

310   well as the highest 2016 CO values, in both MOPITT and MLS observations (Fig. 9). This is consistent

311   with large biomass burning emissions from southern hemisphere (SH) Africa transported into the tropical

312   Atlantic. While SH Africa has the largest magnitude of biomass burning, its relative variability is smaller

Atmospheric
Chemistry
and Physics
Discussions

313   than for the other regions (Fig. 9b). Similarly, the IAV in the MOPITT CO column and 700 hPa level over

314   tropical Atlantic is smaller than that of the North Atlantic and Alaska regions. Although the variability of

315   CO over tropical Atlantic is relatively small, the MOPPIT CO column shows a statistically significant anti-

316   correlation between the MOPITT CO column over the tropical Atlantic and the MEI (r=-0.52). This

317   relationship is not significant for the MOPITT 700 hPa level.

318   The time series of August MOPITT CO columns for both the North Atlantic and Alaska, regions

319   that show high variability, show a small but significant temporal correlation with summertime Siberian

320   biomass burning (r=0.52 for the North Atlantic and r=0.59 for Alaska). Slightly lower values are seen for

321   the 700 hPa MOPITT level. The time series of August MOPITT 700 hPa CO shows an increase in 2003

322   for the North Atlantic and in 2002 and 2003 for Alaska (Fig. 10b,c). Previous studies attribute peaks in

323   these years to the presence of large forest fires in western Russia and Siberia, respectively (Edwards et al.,

324   2004;Yashiro et al., 2009;van der Werf et al., 2006). MOPITT CO values were below average in 2016 for

325   both the North Atlantic and Alaska even though Siberian biomass burning was above average in 2016 (Fig.

326   9a, b).

327   Since ENSO is known to drive large biomass burning variability in Indonesia (*van der Werf et al.*,

328   2006), we consider whether it may influence CO concentrations over the New Zealand region. Although

329   the MOPITT CO column over the Indonesia region does correlate with the MEI (r=0.64), there is no

330   significant correlation between June-Aug biomass burning in Indonesia and MOPITT CO over New

331   Zealand. However, August is not the peak season for Indonesian biomass burning (*Duncan et al.*, 2003b).

332   The large Indonesian fires that occurred during the strong 1997/1998 El Nino peaked during September to

333   November (*Duncan et al.*, 2003a) and active fire detections for the 2015 Indonesian fires peaked in

334   September and October (*Field et al.*, 2016). Thus we might expect Indonesian biomass burning variability

335   to have a greater influence on CO variability during the autumn season, which was sampled in ATom-3.

336   How does 2016 compare to previous years? The MOPITT CO column shows tropical Atlantic CO

337   was near the 75th percentile, while the 700 hPa MOPITT level shows it close to the median. This difference

338   arises because the MOPITT column also includes information from the upper troposphere, and the

339   MOPITT 200 hPa level (not shown) suggests CO levels for 2016 were near the 75th percentile. In contrast,

340   MLS shows that 2016 CO in the upper troposphere was much lower than average, near the 25th percentile.

341   The MOPITT v6 TIR product has a small positive bias drift in the upper troposphere of 0.78 % yr-1 for the

342   200 hPa level (*Deeter et al.*, 2014), which may contribute to the higher rank of 2016 in the MOPITT upper

343   tropospheric data compared to MLS. It is therefore hard to argue that 2016 was outside of the normal IAV

344   for this region.

345   2016 CO in the North Atlantic and Alaska regions was below average in both the MOPITT

346   column and the 700 hPa level, and is in fact the lowest August value in the MOPITT record for the 700 hPa

347   level over Alaska. MLS also shows moderately low CO in the upper troposphere over Alaska in Aug.

348   2016. Combined, this data suggests that the ATom-1 CO is not typical for the region. August 2016 CO

349   column values are also below the median over New Zealand and the eastern and central tropical Pacific, but

Atmospheric
Chemistry
and Physics
Discussions

350   the relatively low variability of these regions makes this less of a concern for the representativeness of the

351   ATom measurements. The IAV of these regions is larger for the MOPITT 700 hPa level, and 2016 lies

352   slightly below the 25th percentile for this level.

353   The regionally-averaged 500 nm AOT from MODIS (Fig. 11) shows similar features to the

354   MOPITT column. The highest values are found for the tropical Atlantic, followed by the Alaska and North

355   Atlantic regions. However, the difference between the tropical Atlantic and the other regions is larger in

356   the aerosol case, while the difference between the North Atlantic and the Pacific regions is smaller. There

357   is also greater relative year-to-year variability over the tropical Atlantic for the aerosols than for CO. The

358   shorter lifetime of aerosols compared to CO, as well as the large contribution from biomass burning, likely

359   explains the greater prominence of the tropical Atlantic in the aerosol case. Furthermore, AOD (Fig. 12)

360   shows a clear peak in 2009 in several of the regions, whereas MOPITT data is missing for Aug. 2009, but

361   MLS shows a minimum (Tropical Atlantic) or no anomaly (other regions).

362   In summary, the multi-year satellite record shows considerable variability in CO, particularly over the

363   North Atlantic and Alaska. Concentrations during August 2016 were on the low end of the distribution for

364   most regions, especially in the lower troposphere. *Worden et al.* (2013) showed negative trends in the

365   MOPITT CO column significant at the one-sigma level for both the Northern and Southern hemispheres for

366   2000-2012. In addition, *Deeter et al.* (2014) report a small negative bias drift in the MOPITT V6 TIR

367   product in the lower troposphere, although drift in the column is almost negligible. Decreasing MOPITT

368   CO over time is also visible in some regions in Fig. 10. This negative trend may be contributing to the low

369   values in 2016. Overall, the year 2016 shows anomalies for some regions, but does not appear to be an

370   extreme year.

371   **6   Conclusions**

372   We place the observations from the ATom-1 campaign in the context of interannual variability and

373   global source distributions using satellite observations and tagged tracers from GEOS-5, respectively.

374   GEOS-5 gives a reasonable reproduction of the background CO levels for most flights despite the use of

375   climatological fossil fuel and biofuel emissions, and captures the global distribution of CO observed during

376   ATom-1. Simulations with both forecast and analysis winds capture the timing of many of the enhanced

377   CO plumes encountered during the flights, although the magnitude of the enhancements was often

378   underestimated, which is not unexpected given the difference in resolution between the observations and

379   model. The strong performance of GEOS-5 with regards to the overall CO distribution and the timing of

380   the enhancements gives us confidence in using tagged tracers to identify the sources affecting the air

381   sampled in ATom-1.

382   We find that for most flights the dominant contribution to total CO is from non-biomass burning

383   sources, which include both fossil fuels and biofuels and oxidation of hydrocarbons including methane. An

384   exception to this is in the lower troposphere of the tropical Atlantic, where biomass burning from Africa

385   makes the largest contribution, exceeding 100 ppb in some locations. The non-BB source includes a large

Atmospheric
Chemistry
and Physics
Discussions

386   fraction from Asia for flights over the North Pacific and from both Asia and North America for the North

387   Atlantic and North American flights, while other regions dominate in the Southern Hemisphere. Plumes of

388   elevated CO from both biomass burning and non-BB sources led to observations of enhanced CO during

389   ATom-1.

390   We use satellite observations of CO from MOPITT and MLS and AOT from MODIS to assess

391   whether August 2016, the period sampled by ATom-1, is typical or atypical in the context of IAV in the

392   satellite record (2000-2016). MOPITT and MLS show that CO in the lower and upper troposphere,

393   respectively, were below average in August 2016 compared to the satellite record for August for most of

394   the regions sampled by ATom-1, but not usually the minimum year. CO concentrations in the North

395   Atlantic and Alaskan regions show a positive correlation with Siberian biomass burning and large

396   interannual variability. In contrast, both MODIS AOT and the MOPITT CO column show above average

397   values for the Tropical Atlantic in 2016. This suggests that the high values of CO and aerosols from

398   biomass burning encountered during the tropical Atlantic portions of ATom may have been especially

399   pronounced during this particular year.

400   The seasonality of biomass burning, the OH distribution, and atmospheric transport pathways can

401   alter the source contributions from season to season. Thus, the next three ATom campaigns, which occur

402   in different seasons, will likely show variations in the relative source contributions to each region.

403

Data Availability

405   Data from ATom-1 is available on the ESPO archive

406   (https://espo.nasa.gov/home/atom/archive/browse/atom). MOPITT data is available at

407   https://eosweb.larc.nasa.gov/datapool. MLS data is available from https://mls.jpl.nasa.gov/. MODIS

408   aerosol data are available from

409   https://ladsweb.modaps.eosdis.nasa.gov/api/v1/productGroupPage/name=aerosol.

410

414

415

References

417   ATom Science Team (2017), Moffett Field, CA, NASA Ames Earth Science Project Office (ESPO),

418   Accessed at doi: 10.5067/Aircraft/ATom/TraceGas_Aerosol_Global_Distribution

419   Bian, H., Colarco, P., Chin, M., Chen, G., Rodriguez, J., Liang, Q., Blake, D., Chu, D., da Silva, A.,

420   Darmenov, A., Diskin, G., Fuelberg, H., Huey, G., Kondo, Y., Nielsen, J., Pan, X., and Wisthaler, A.:

421   Source attributions of pollution to the Western Arctic during the NASA ARCTAS field campaign,

422   Atmospheric Chemistry and Physics, 13, 4707-4721, 10.5194/acp-13-4707-2013, 2013.

Atmospheric
Chemistry
and Physics
Discussions

423   e.d. Blunden, J., and D. S. Arndt: State of the Climate in 2015. In: *Bull. Amer. Meteor. Soc.*, 97(8), 2016.

424   Darmenov, A. and A. da Silva, The Quick Fire Emissions Dataset (QFED): Documentation of versions 2.1,

425   2.2 and 2.4. NASA/TM–2015–104606, Vol. 38, 2015.

426   Deeter, M., Martinez-Alonso, S., Edwards, D., Emmons, L., Gille, J., Worden, H., Sweeney, C., Pittman, J.,

427   Daube, B., and Wofsy, S.: The MOPITT Version 6 product: algorithm enhancements and validation,

428   Atmospheric Measurement Techniques, 7, 3623-3632, 10.5194/amt-7-3623-2014, 2014.

429   Duncan, B., Bey, I., Chin, M., Mickley, L., Fairlie, T., Martin, R., and Matsueda, H.: Indonesian wildfires

430   of 1997: Impact on tropospheric chemistry, Journal of Geophysical Research-Atmospheres, 108,

431   10.1029/2002JD003195, 2003a.

432   Duncan, B. N., Martin, R. V., Staudt, A. C., Yevich, R., and Logan, J. A.: Interannual and seasonal

433   variability of biomass burning emissions constrained by satellite observations, Journal of Geophysical

434   Research-Atmospheres, 108, 10.1029/2002jd002378, 2003b.

435   Duncan, B. N., and Logan, J. A.: Model analysis of the factors regulating the trends and variability of

436   carbon monoxide between 1988 and 1997, Atmospheric Chemistry and Physics, 8, 7389-7403, 2008.

437   Edwards, D., Petron, G., Novelli, P., Emmons, L., Gille, J., and Drummond, J.: Southern Hemisphere

438   carbon monoxide interannual variability observed by Terra/Measurement of Pollution in the Troposphere

439   (MOPITT), Journal of Geophysical Research-Atmospheres, 111, 10.1029/2006JD007079, 2006.

440   Edwards, D. P., Emmons, L. K., Hauglustaine, D. A., Chu, D. A., Gille, J. C., Kaufman, Y. J., Petron, G.,

441   Yurganov, L. N., Giglio, L., Deeter, M. N., Yudin, V., Ziskin, D. C., Warner, J., Lamarque, J. F., Francis,

442   G. L., Ho, S. P., Mao, D., Chen, J., Grechko, E. I., and Drummond, J. R.: Observations of carbon monoxide

443   and aerosols from the Terra satellite: Northern Hemisphere variability, Journal of Geophysical Research-

444   Atmospheres, 109, 10.1029/2004jd004727, 2004.

445   Emmons, L., Pfister, G., Edwards, D., Gille, J., Sachse, G., Blake, D., Wofsy, S., Gerbig, C., Matross, D.,

446   and Nedelec, P.: Measurements of Pollution in the Troposphere (MOPITT) validation exercises during

447   summer 2004 field campaigns over North America, Journal of Geophysical Research-Atmospheres, 112,

448   10.1029/2006JD007833, 2007.

449   Field, R., van der Werf, G., Fanin, T., Fetzer, E., Fuller, R., Jethva, H., Levy, R., Livesey, N., Luo, M.,

450   Torres, O., and Worden, H.: Indonesian fire activity and smoke pollution in 2015 show persistent nonlinear

451   sensitivity to El Nino-induced drought, Proceedings of the National Academy of Sciences of the United

452   States of America, 113, 9204-9209, 10.1073/pnas.1524888113, 2016.

453   Heald, C., Jacob, D., Fiore, A., Emmons, L., Gille, J., Deeter, M., Warner, J., Edwards, D., Crawford, J.,

454   Hamlin, A., Sachse, G., Browell, E., Avery, M., Vay, S., Westberg, D., Blake, D., Singh, H., Sandholm, S.,

455   Talbot, R., and Fuelberg, H.: Asian outflow and trans-Pacific transport of carbon monoxide and ozone

456   pollution: An integrated satellite, aircraft, and model perspective, Journal of Geophysical Research-

457   Atmospheres, 108, 10.1029/2003JD003507, 2003.

458   Hsu, J., Prather, M., Wild, O., Sundet, J., Isaksen, I., Browell, E., Avery, M., and Sachse, G.: Are the
459   TRACE-P measurements representative of the western Pacific during March 2001?, Journal of Geophysical
460   Research-Atmospheres, 109, 10.1029/2003JD004002, 2004.

461   Kasischke, E., Hyer, E., Novelli, P., Bruhwiler, L., French, N., Sukhinin, A., Hewson, J., and Stocks, B.:
462   Influences of boreal fire emissions on Northern Hemisphere atmospheric carbon and carbon monoxide,
463   Global Biogeochemical Cycles, 19, 10.1029/2004GB002300, 2005.

464   Langenfelds, R., Francey, R., Pak, B., Steele, L., Lloyd, J., Trudinger, C., and Allison, C.: Interannual
465   growth rate variations of atmospheric CO2 and its delta C-13, H-2, CH4, and CO between 1992 and 1999
466   linked to biomass burning, Global Biogeochemical Cycles, 16, 10.1029/2001GB001466, 2002.

467   Levy, R., Hsu, C., et al.: MODIS Atmosphere L2 Aerosol Product. NASA MODIS Adaptive Processing
468   System, Goddard Space Flight Center, USA, doi:http://dx.doi.org/10.5067/MODIS/MYD04_L2.006, 2015.

469   Liu, J., J. A. Logan, L. T. Murray, H. C. Pumphrey, and I. A. Megretskaia, Transport analysis and source
470   attribution of seasonal and interannual variability of CO in the tropical upper troposphere and lower
471   stratosphere. *Atmos. Chem. Phys.*, **13:** 129-146 doi:10.5194/acp-13-129-2013, 2013.

472   Livesey, N., Filipiak, M., Froidevaux, L., Read, W., Lambert, A., Santee, M., Jiang, J., Pumphrey, H.,
473   Waters, J., Cofield, R., Cuddy, D., Daffer, W., Drouin, B., Fuller, R., Jarnot, R., Jiang, Y., Knosp, B., Li,
474   Q., Perun, V., Schwartz, M., Snyder, W., Stek, P., Thurstans, R., Wagner, P., Avery, M., Browell, E.,
475   Cammas, J., Christensen, L., Diskin, G., Gao, R., Jost, H., Loewenstein, M., Lopez, J., Nedelec, P.,
476   Osterman, G., Sachse, G., and Webster, C.: Validation of Aura Microwave Limb Sounder O-3 and CO
477   observations in the upper troposphere and lower stratosphere, Journal of Geophysical Research-
478   Atmospheres, 113, 10.1029/2007JD008805, 2008.

479   Logan, J., Megretskaia, I., Nassar, R., Murray, L., Zhang, L., Bowman, K., Worden, H., and Luo, M.:
480   Effects of the 2006 El Nino on tropospheric composition as revealed by data from the Tropospheric
481   Emission Spectrometer (TES), Geophysical Research Letters, 35, 10.1029/2007GL031698, 2008.

482   Lucchesi, R, File Specification for GEOS-5 FP. GMAO Office Note No. 4 (Version 1.1), 61pp, 2017,
483   available from http://gmao.gsfc.nasa.gov/pubs/office_notes.

484   Molod, A., Takacs, L., Suarez, M., and Bacmeister, J.: Development of the GEOS-5 atmospheric general
485   circulation model: evolution from MERRA to MERRA2, Geoscientific Model Development, 8, 1339-1356,
486   10.5194/gmd-8-1339-2015, 2015.

487   Novelli, P., Masarie, K., Lang, P., Hall, B., Myers, R., and Elkins, J.: Reanalysis of tropospheric CO trends:
488   Effects of the 1997-1998 wildfires, Journal of Geophysical Research-Atmospheres, 108,
489   10.1029/2002JD003031, 2003.

490   Ott, L., Duncan, B., Pawson, S., Colarco, P., Chin, M., Randles, C., Diehl, T., and Nielsen, E.: Influence of
491   the 2006 Indonesian biomass burning aerosols on tropical dynamics studied with the GEOS-5 AGCM,
492   Journal of Geophysical Research-Atmospheres, 115, 10.1029/2009jd013181, 2010.

493   Pfister, G., Emmons, L., Edwards, D., Arellano, A., Sachse, G., and Campos, T.: Variability of springtime
494   transpacific pollution transport during 2000-2006: the INTEX-B mission in the context of previous years,
495   Atmospheric Chemistry and Physics, 10, 1345-1359, 10.5194/acp-10-1345-2010, 2010.
496   Prather, M., Zhu, X., Flynn, C., Strode, S., Rodriguez, J., Steenrod, S., Liu, J., Lamarque, J., Fiore, A.,
497   Horowitz, L., Mao, J., Murray, L., Shindell, D., and Wofsy, S.: Global atmospheric chemistry - which air
498   matters, Atmospheric Chemistry and Physics, 17, 9081-9102, 10.5194/acp-17-9081-2017, 2017.
499   Reinecker, M. M. et al., The GEOS-5 Data Assimilation System – Documentation of Versions 5.0.1, 5.1.0,
500   and 5.2.0, Technical Report Series on Global Modeling and Data Assimilation, Vol. 27, ed. M. J. Suarez,
501   NASA/TM-2008-104606, 2008.
502   Rienecker, M. M., Suarez, M. J., Gelaro, R., Todling, R., Bacmeister, J., Liu, E., Bosilovich, M. G.,
503   Schubert, S. D., Takacs, L., Kim, G.-K., Bloom, S., Chen, J., Collins, D., Conaty, A., da Silva, A., Gu, W.,
504   Joiner, J., Koster, R. D., Lucchesi, R., Molod, A., Owens, T., Pawson, S., Pegion, P., Redder, C. R.,
505   Reichle, R., Robertson, F. R., Ruddick, A. G., Sienkiewicz, M., and Woollen, J.: MERRA: NASA's
506   Modern-Era Retrospective Analysis for Research and Applications, Journal of Climate, 24, 3624-3648,
507   10.1175/JCLI-D-11-00015.1, 2011.
508   Santoni, G., Daube, B., Kort, E., Jimenez, R., Park, S., Pittman, J., Gottlieb, E., Xiang, B., Zahniser, M.,
509   Nelson, D., McManus, J., Peischl, J., Ryerson, T., Holloway, J., Andrews, A., Sweeney, C., Hall, B.,
510   Hintsa, E., Moore, F., Elkins, J., Hurst, D., Stephens, B., Bent, J., and Wofsy, S.: Evaluation of the airborne
511   quantum cascade laser spectrometer (QCLS) measurements of the carbon and greenhouse gas suite - CO2,
512   CH4, N2O, and CO - during the CalNex and HIPPO campaigns, Atmospheric Measurement Techniques, 7,
513   1509-1526, 10.5194/amt-7-1509-2014, 2014.
514   Strode, S. A., and Pawson, S.: Detection of carbon monoxide trends in the presence of interannual
515   variability, Journal of Geophysical Research-Atmospheres, 118, 12257-12273, 10.1002/2013JD020258,
516   2013.
517   van der Werf, G., Randerson, J., Giglio, L., Collatz, G., Kasibhatla, P., and Arellano, A.: Interannual
518   variability in global biomass burning emissions from 1997 to 2004, Atmospheric Chemistry and Physics, 6,
519   3423-3441, 2006.
520   Voulgarakis, A., Marlier, M., Faluvegi, G., Shindell, D., Tsigaridis, K., and Mangeon, S.: Interannual
521   variability of tropospheric trace gases and aerosols: The role of biomass burning emissions, Journal of
522   Geophysical Research-Atmospheres, 120, 7157-7173, 10.1002/2014JD022926, 2015.
523   Waters, J., Froidevaux, L., Harwood, R., Jarnot, R., Pickett, H., Read, W., Siegel, P., Cofield, R., Filipiak,
524   M., Flower, D., Holden, J., Lau, G., Livesey, N., Manney, G., Pumphrey, H., Santee, M., Wu, D., Cuddy,
525   D., Lay, R., Loo, M., Perun, V., Schwartz, M., Stek, P., Thurstans, R., Boyles, M., Chandra, K., Chavez,
526   M., Chen, G., Chudasama, B., Dodge, R., Fuller, R., Girard, M., Jiang, J., Jiang, Y., Knosp, B., LaBelle, R.,
527   Lam, J., Lee, K., Miller, D., Oswald, J., Patel, N., Pukala, D., Quintero, O., Scaff, D., Van Snyder, W.,
528   Tope, M., Wagner, P., and Walch, M.: The Earth Observing System Microwave Limb Sounder (EOS MLS)

529 on the Aura satellite, Ieee Transactions on Geoscience and Remote Sensing, 44, 1075-1092,

530 10.1109/TGRS.2006.873771, 2006.

531 Wolter, K., and Timlin, M. S.: Monitoring ENSO in COADS with a seasonally adjusted principal

532 component index, Proc. of the 17th Climate Diagnostics Workshop, 1993,

533 Worden, H. M., Deeter, M. N., Frankenberg, C., George, M., Nichitiu, F., Worden, J., Aben, I., Bowman,

534 K. W., Clerbaux, C., Coheur, P. F., de Laat, A. T. J., Detweiler, R., Drummond, J. R., Edwards, D. P.,

535 Gille, J. C., Hurtmans, D., Luo, M., Martinez-Alonso, S., Massie, S., Pfister, G., and Warner, J. X.: Decadal

536 record of satellite carbon monoxide observations, Atmospheric Chemistry and Physics, 13, 837-850,

537 10.5194/acp-13-837-2013, 2013.

538 Yashiro, H., Sugawara, S., Sudo, K., Aoki, S., and Nakazawa, T.: Temporal and spatial variations of carbon

539 monoxide over the western part of the Pacific Ocean, Journal of Geophysical Research-Atmospheres, 114,

540 10.1029/2008JD010876, 2009.

541 Ziemke, J., and Chandra, S.: La Nina and El Nino-induced variabilities of ozone in the tropical lower

542 atmosphere during 1970-2001, Geophysical Research Letters, 30, 10.1029/2002GL016387, 2003.

543

Atmospheric
Chemistry
and Physics
Discussions

544   **Table 1 : Regional August 2016 CO Emission Totals in the GEOS-5 FP Simulations**

	Fossil Fuel[1]	Biogenic[1]	BB[1]
North America	6.7	5.8	2.4
Europe	4.9	2.4	
Asia	26	7.9	
Eurasia[2]			3.0
Africa			24
South America	13	17	11
Other[3]			2.9
Global	50	34	43

545   [1]Emissions are in units of Tg.

546   [2]The Eurasian tagged tracer for BB CO includes emissions from Europe and northern Asia, but excludes

547   southern Asia.

548   [3]Other fossil fuel emissions includes emissions from Africa and South America, while other BB emissions

549   excludes those regions since they are tagged separately.

550

551   **Table 2: Mean and Standard Deviations in CO along Atlantic and Pacific Flight Tracks**

Region	Flight	Obs Mean (ppb)	Obs Stdev (ppb)	Model Mean (ppb)	Model Stdev (ppb)
Eastern Pacific	1. Palmdale – Palmdale	75	14	77	19
	2. Palmdale - Anchorage	100	40	88	16
Pacific	3. Anchorage-Kona	85	36	81	18
	4. Kona –Pago Pago	61	5.1	63	5.5
	5. Pago Pago – Christchurch	55	11	57	6.1
Southern Ocean	6. Christchurch – Punta Arenas	56	6.4	54	4.7
Atlantic	7. Punta Arenas – Ascension	69	17	71	26
	8. Ascension – Azores	101	36	103	27
	9. Azores – Kangerlussuaq	88	32	87	19

Atmospheric
Chemistry
and Physics
Discussions

N. America	10. Kangerlussuaq – Minneapolis	90	26	91	22
	11. Minneapolis – Palmdale	84	38	107	78

552
553

554

555


556
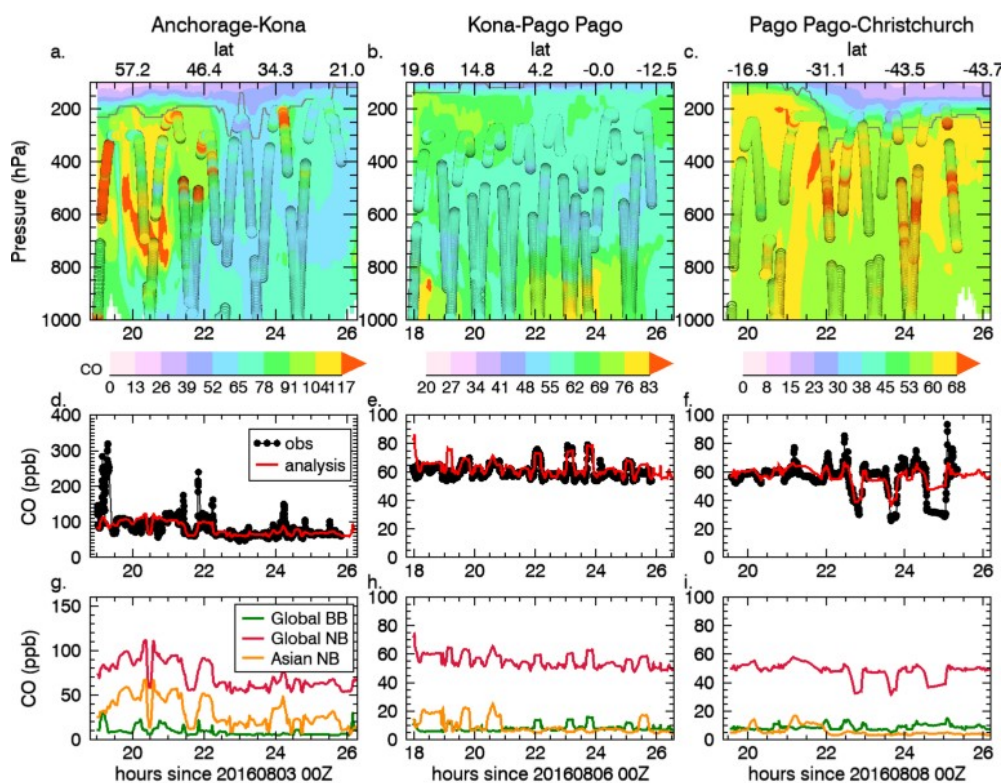
Figure 1: Curtain plot of CO (ppb) from the GEOS-5 analysis as a function of time and pressure overplotted with the model tropopause (gray line) and QCLS CO observations (circles) (top row) for the a) Anchorage to Kona flight, b) Kona to Pago Pago flight, and c) Pago Pago to Christchurch flight. Axis ranges vary between panels due to the large range of concentrations encountered. The top x-axis indicates the latitudes of the flight track. d-f) The GEOS-5 CO interpolated to the flight track (red line) is compared to the observations (black circles). g-h) Tagged tracer contributions to the GEOS-5 CO.

563
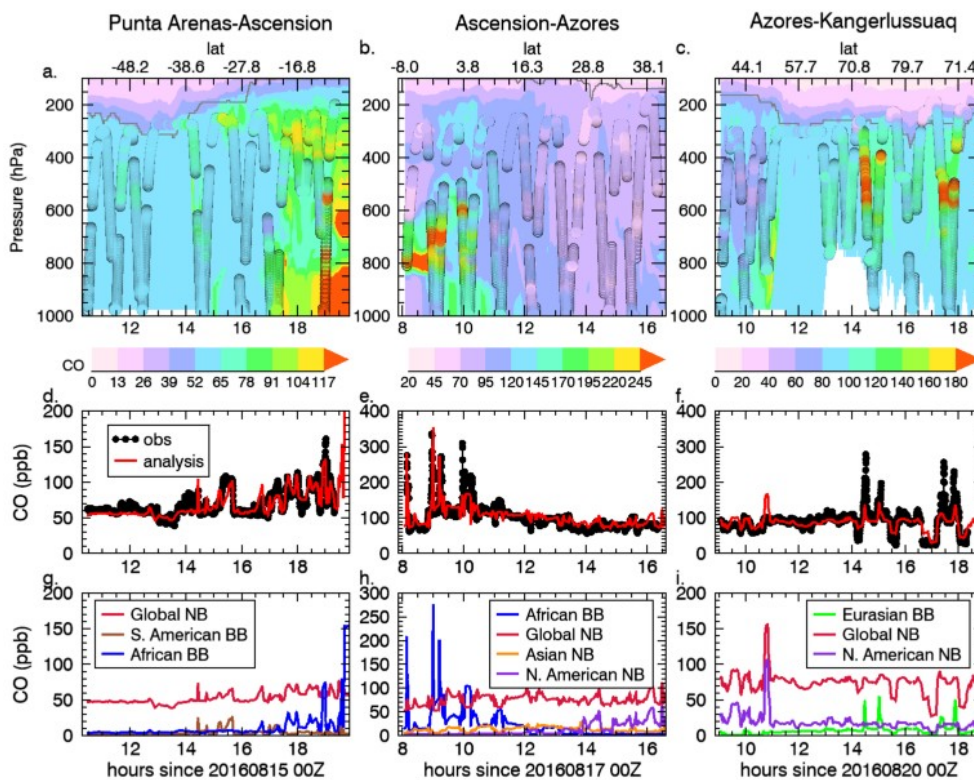
Figure 2: As in Fig. 1, but for the Atlantic flights: a,d,g) Punta Arenas-Ascension Island, b,e,h) Ascension Island to the Azores, and c,f,i) Azores to Kangerlussuaq.

566
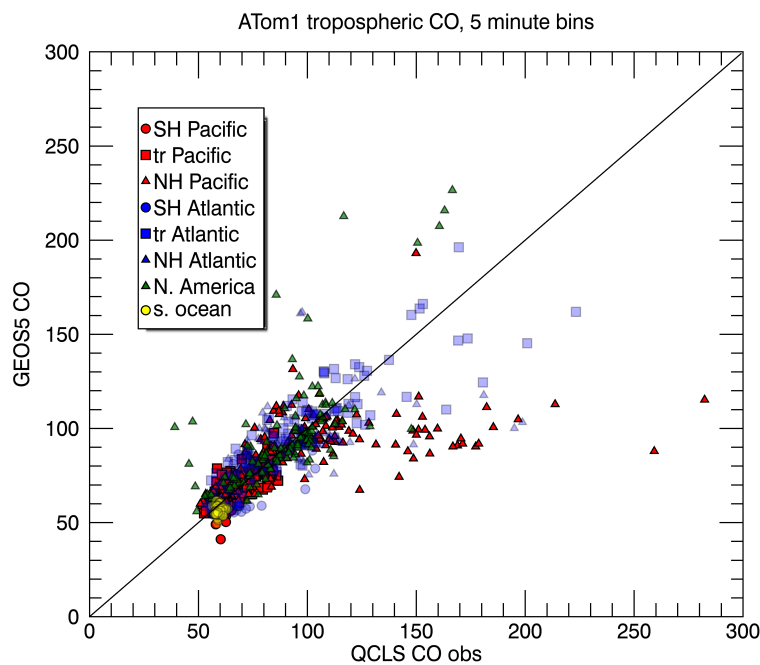
Figure 3: GEOS-5 simulated CO versus QCLS CO observations for all ATom-1 flights averaged into 5 minute bins. CO is in units of ppb. Pacific flights are shown in red, Atlantic flights in blue, N. American flights in green, and southern ocean flights in yellow. Circles indicate Southern Hemisphere points, triangles indicate Northern Hemisphere points, and squares indicate tropical points. The one-to-one line is overplotted in black.

571
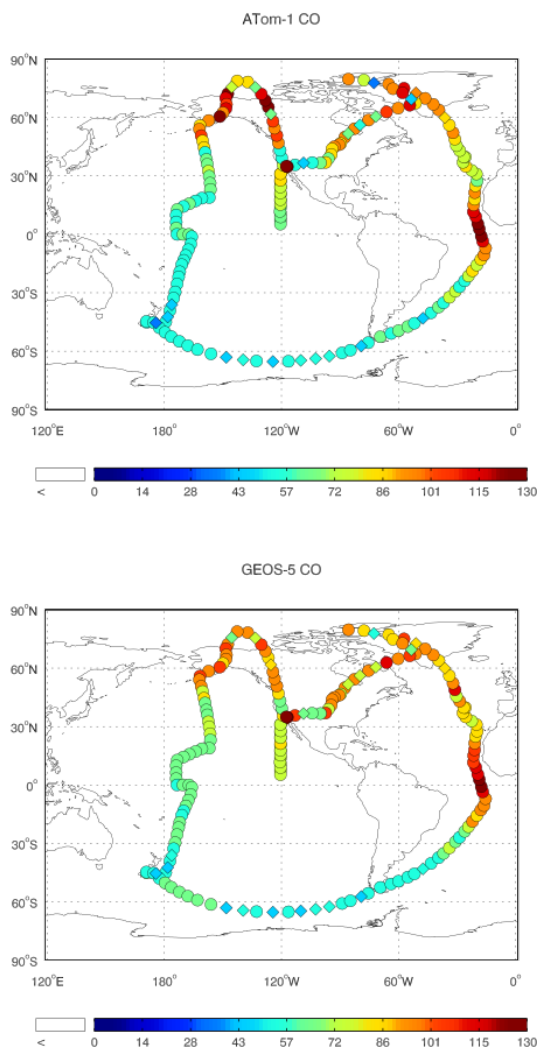
Figure 4: CO (ppb) from the QCLS observations (top) and GEOS-5 analysis (bottom) for the ATom-1 circuit including all 11 research flight segments. The GEOS-5 CO is taken from the analysis closest to the mid-point of the flight time and interpolated to the flight track following the longitude, latitude and pressure given in the observations. Both model forecast and ATom measurements are averaged into a sample rate of one per 360-second. Data in the troposphere are plotted in a circle, while data in the stratosphere are plotted in a diamond, based on the GEOS-5 tropopause.

579

Atmospheric
Chemistry
and Physics
Discussions

Open Access

580
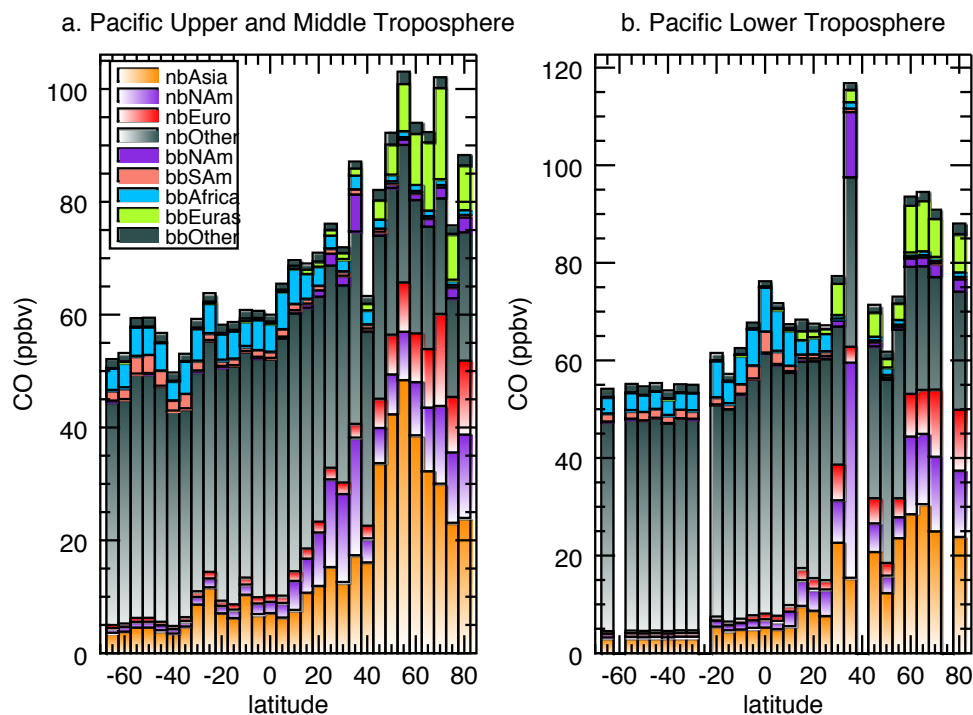
Figure 5: The contribution of each tagged CO tracer over the Pacific in the (a) upper and middle troposphere
(pressure <= 850 hPa) and (b) lower troposphere (pressure > 850 hPa). Data from multiple flights over the
region between 120°E and 110°W is included, with each bar representing data averaged over a 5 degree latitude
bin. Shaded bars represent non-BB CO from Asia (orange), N. America (purple), Europe (red), and the rest of
the world (gray). Solid bars represent BB CO from N. America (purple), S. America (pink), Africa (cyan),
Eurasia (green), and the rest of the world (gray).
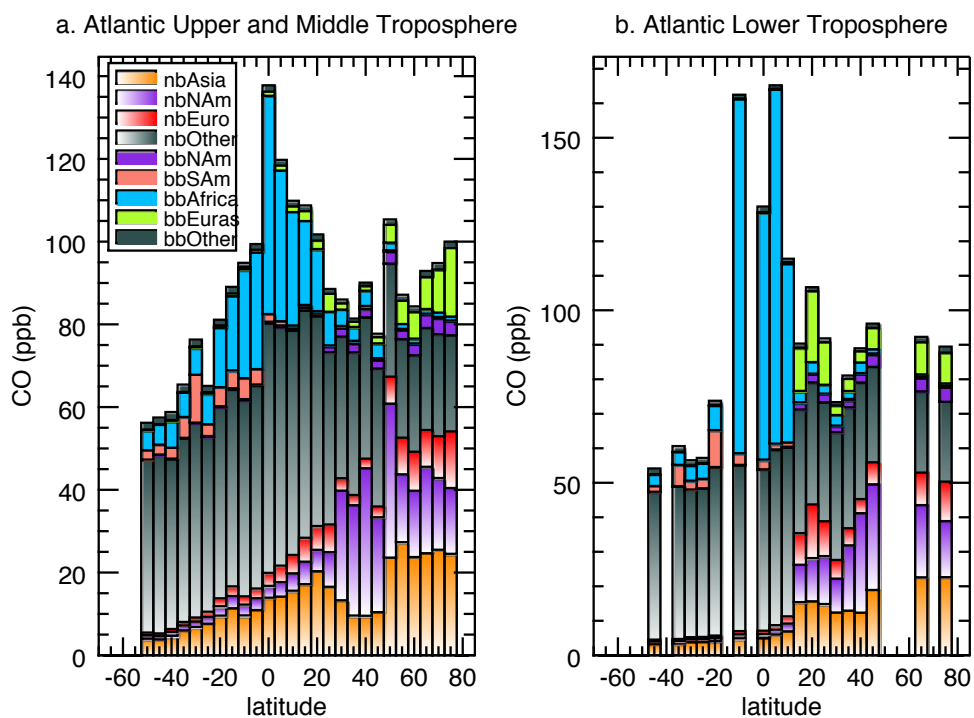
Figure 6: As in Fig. 5, but for the Atlantic. Data from multiple flights over the region 0-60°W is included, with each bar representing data averaged over a 5 degree latitude bin.
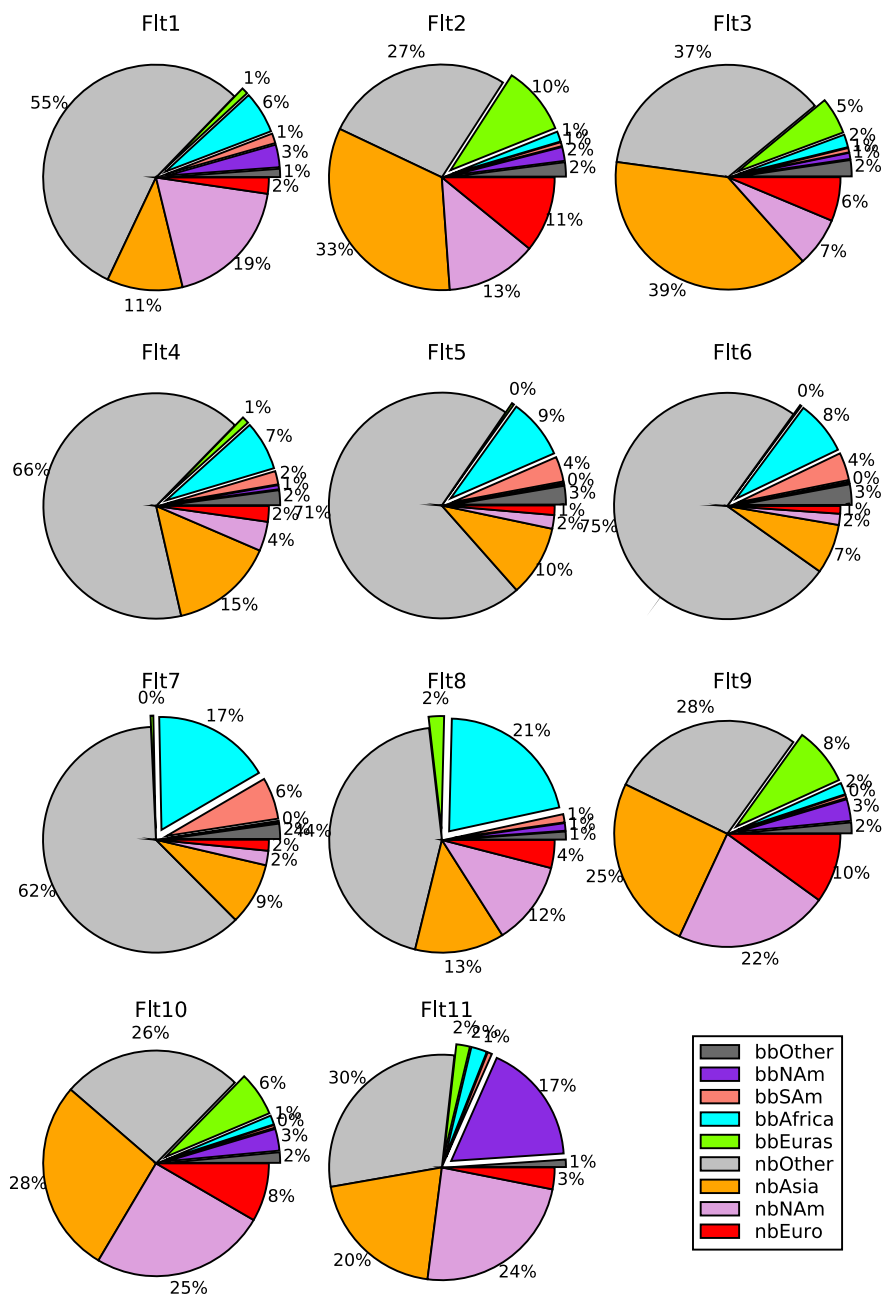
Figure 7: Percent contributions of tagged tracers to total CO for each flight. Exploded slices represent the
biomass burning tracers: North American (purple), S. American (salmon), African (cyan), Eurasian (green), and

Atmospheric
Chemistry
and Physics
Discussions

Open Access

EGU

593   Other (dark gray). The non-biomass burning (nb) tracers are for Asia (orange), N. America (lavender), Europe
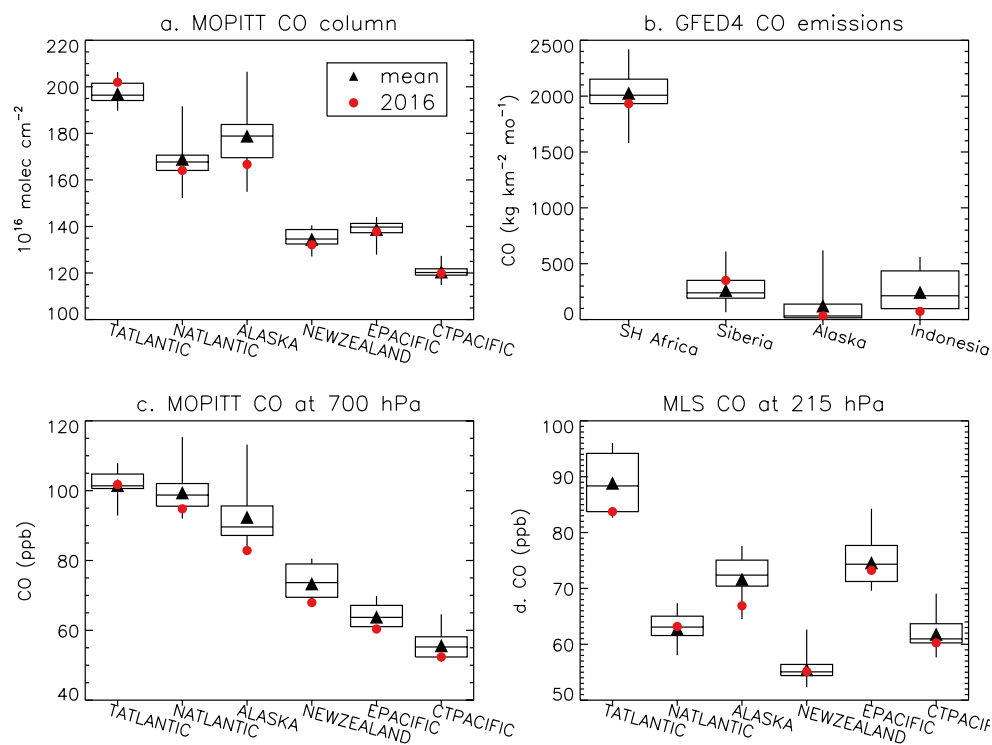594   (red), and other (light gray).

595

596
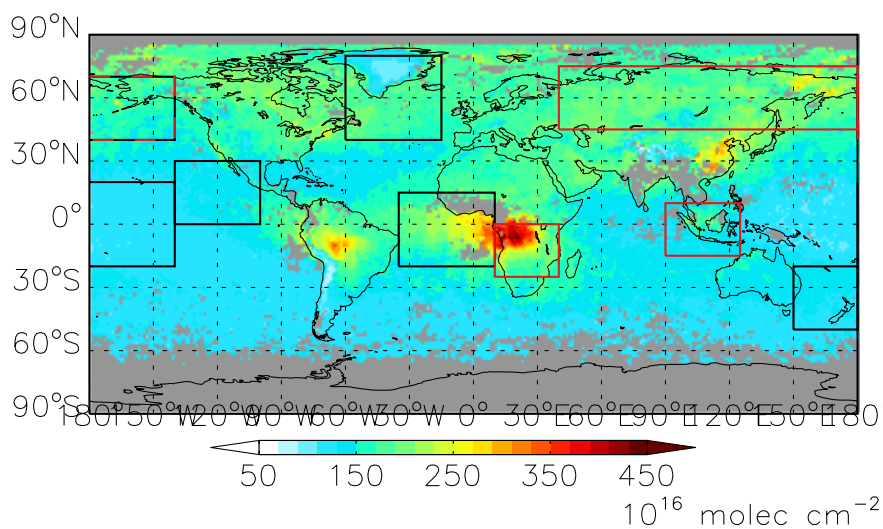
597

598

599   Figure 8: MOPITT CO column for August 2016 overplotted with the regions shown in Fig. 10. Black rectangles
600   indicate the regions where we analyze CO concentrations, and red rectangles indicate the regions used for
601   biomass burning.

Atmospheric
Chemistry
and Physics
Discussions

602

Figure 9: Boxes show the 25th, 50th, and 75th percentile values; whiskers show the minimum and maximum values; black triangles show the mean value, and red circles show the 2016 value for a) the MOPITT CO column, b) the GFED4 CO emissions, c) MOPITT CO at 700 hPa, and d) MLS CO at 215 hPa. Statistics for MOPITT are for 2000-2016, statistics for GFED4 are for 2000-2015, and statistics for MLS are for 2004-2016. MOPITT and MLS values are for August, while the GFED4 emissions are averaged over June through August.
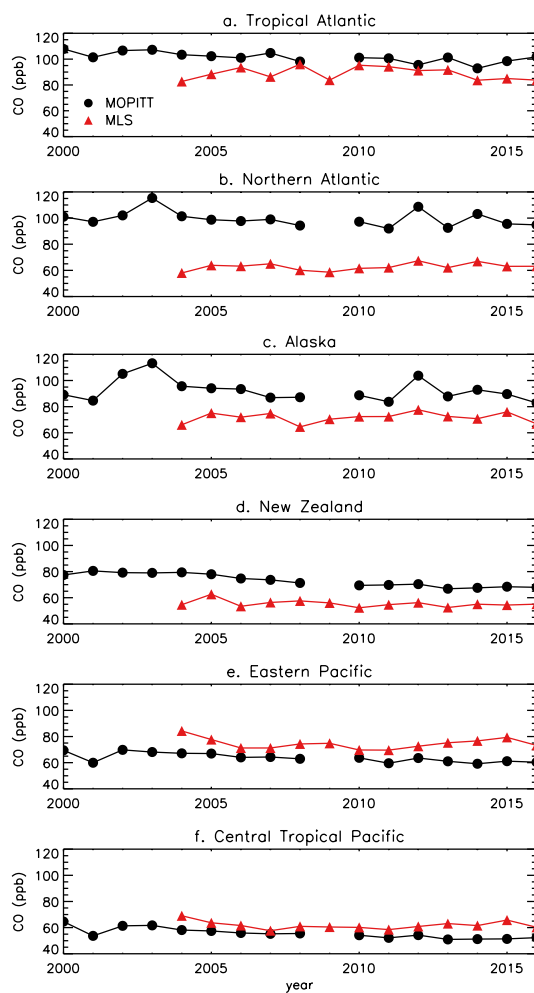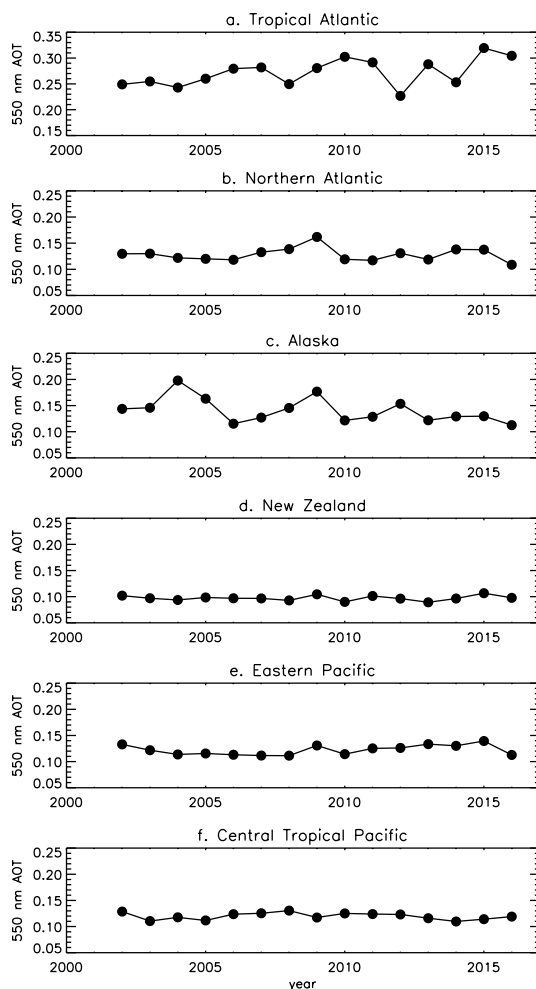
608

609

610 **Figure 10: Time series of August MOPITT CO at the 700 hPa level (black circles) and MLS CO (red triangles)**
611 **at the 215 hPa level for the 6 regions shown in black in Fig. 8.**

Atmospheric
Chemistry
and Physics
Discussions

612
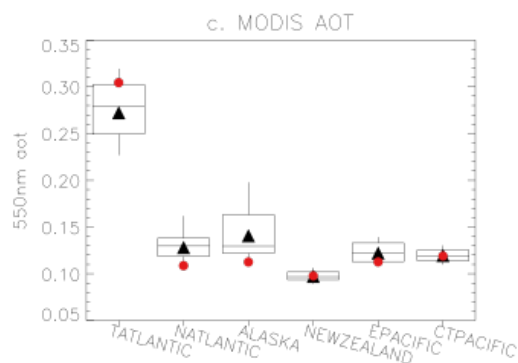
Figure 11: As in Figure 9, but for the MODIS 550 nm AOT. Only values over oceans are included in the regional averages.

615
Figure 12: Time series of regionally averaged MODIS 550 nm AOT. Only values over oceans are included in the

617   regional averages. The y-axis range for panel a differs from the other panels due to the higher AOT values in
618   that   region.